First Space-based Microlens Parallax Measurement of an Isolated Star: *Spitzer* Observations of OGLE-2014-BLG-0939

J. C. Yee[1], A. Udalski[2], S. Calchi Novati[3,4,5], A. Gould[6], S. Carey[7], R. Poleski[2,6], B.S. Gaudi[6], R.W. Pogge[6] J. Skowron[2], S. Kozłowski[2], P. Mróz[2], P. Pietrukowicz[2], G. Pietrzyński[2,8] M.K. Szymański[2], I. Soszyński[2], K. Ulaczyk[2], Ł. Wyrzykowski[2,9]

[1]Harvard-Smithsonian Center for Astrophysics, 60 Garden St., Cambridge, MA 02138, USA

[2]Warsaw University Observatory, Al. Ujazdowskie 4, 00-478 Warszawa, Poland

[3]NASA Exoplanet Science Institute, MS 100-22, California Institute of Technology, Pasadena, CA 91125, USA[1]

[4]Dipartimento di Fisica "E. R. Caianiello", Università di Salerno, Via Giovanni Paolo II, 84084 Fisciano (SA), Italy

[5]Istituto Internazionale per gli Alti Studi Scientifici (IIASS), Via G. Pellegrino 19, 84019 Vietri Sul Mare (SA), Italy [6]Department of Astronomy, Ohio State University, 140 W. 18th Ave., Columbus, OH 43210, USA

[7]Spitzer Science Center, MS 220-6, California Institute of Technology,Pasadena, CA, USA

[8]Universidad de Concepción, Departamento de Astronomia, Casilla 160–C, Concepción, Chile

[9]Institute of Astronomy, University of Cambridge, Madingley Road, Cambridge CB3 0HA, UK

ABSTRACT

We present the first space-based microlens parallax measurement of an isolated star. From the striking differences in the lightcurve as seen from Earth and from *Spitzer* (~ 1 AU to the West), we infer a projected velocity $\tilde{v}_{\rm hel} \sim 250\,{\rm km\,s^{-1}}$, which strongly favors a lens in the Galactic Disk with mass $M = 0.23 \pm 0.07\,M_\odot$ and distance $D_L = 3.1 \pm 0.4\,{\rm kpc}$. An ensemble of such measurements drawn from our ongoing program could be used to measure the single-lens mass function including dark objects, and also is necessary for measuring the Galactic distribution of planets since the ensemble reflects the underlying Galactic distribution of microlenses. We study the application of the many ideas to break the four-fold degeneracy first predicted by Refsdal 50 years ago. We find that this degeneracy is clearly broken, but by two unanticipated mechanisms.

Subject headings: gravitational lensing: micro

[1]Sagan visiting fellow

1. Introduction

When modern microlensing experiments were proposed toward the Large Magellanic Cloud (Paczyński 1986) and the Galactic Bulge (Paczyński 1991; Griest et al. 1991), it was believed that the only information that could be extracted about the lens mass M, distance D_L, and transverse motion $\boldsymbol{\mu}_{\rm geo}$ would come through their combination in a single measured parameter, the Einstein timescale,

$$t_{\rm E} = \frac{\theta_{\rm E}}{\mu_{\rm geo}}; \qquad \theta_{\rm E}^2 \equiv \kappa M \pi_{\rm rel}; \qquad \kappa \equiv \frac{4G}{c^2 {\rm AU}} \simeq 8.14 \frac{\rm mas}{M_\odot}. \tag{1}$$

Here $\theta_{\rm E}$ is the angular Einstein radius, $\pi_{\rm rel} = {\rm AU}(D_L^{-1} - D_S^{-1})$ is the lens-source relative parallax, and $\mu_{\rm geo}$ is the lens-source relative proper motion in the Earth frame at the peak of the event. This would imply, in particular, that individual masses could be estimated only to within an order of magnitude (e.g., Figure 1 of Gould 2000a).

It was quickly realized, however, that if two additional potentially observable quantities could be measured, $\theta_{\rm E}$ and the "microlens parallax vector" $\boldsymbol{\pi}_{\rm E}$, then these three quantities could be disentangled (Gould 1992),

$$M = \frac{\theta_{\rm E}}{\kappa \pi_{\rm E}}; \qquad \pi_{\rm rel} = \pi_{\rm E} \theta_{\rm E}; \qquad \boldsymbol{\mu}_{\rm geo} = \frac{\theta_{\rm E}}{t_{\rm E}} \frac{\boldsymbol{\pi}_{\rm E,geo}}{\pi_{\rm E}}. \tag{2}$$

In modern notation, the microlens parallax vector is given by (Gould 2000b),

$$\boldsymbol{\pi}_{\rm E} \equiv \frac{\pi_{\rm rel}}{\theta_{\rm E}} \frac{\boldsymbol{\mu}}{\mu}. \tag{3}$$

Its amplitude quantifies the lens-source relative displacement in the Einstein ring due to motion of the observer, while its direction specifies the orientation of this displacement as the event evolves. Hence, $\boldsymbol{\pi}_{\rm E}$ is in principle measurable from photometric deviations of the event relative to what is expected from rectilinear motion. See Figure 1 of Gould & Horne (2013) for a didactic explanation.

While both $\theta_{\rm E}$ and $\boldsymbol{\pi}_{\rm E}$ are important, measurements of $\boldsymbol{\pi}_{\rm E}$ are more pressing for the following three reasons. First, $\theta_{\rm E}$ is very frequently measured "automatically" in planetary and binary events. Hence, $\pi_{\rm E}$ is the crucial missing link to obtain individual masses for these high priority events, i.e., those for which individual masses are the most important. Second, $\theta_{\rm E}$ is very rarely measurable in single-lens events, which means that measuring $\pi_{\rm E}$ is the best way to obtain strong statistical constraints on masses of the much larger population of (dark and luminous) single lenses. Third, while $\pi_{\rm E}$ and $\theta_{\rm E}$ appear symmetrically in Equation (2), $\pi_{\rm E}$ is actually much richer in information than $\theta_{\rm E}$. This is because the great majority of

lenses observed toward the Galactic Bulge have similar proper motions within a factor ~ 2 of $\mu \sim 4\,\mathrm{mas\,yr^{-1}}$. Thus, in the limit that all microlens proper motions had exactly this value, a measurement of $\theta_\mathrm{E} = \mu t_\mathrm{E}$ would contain no additional information, while π_E would completely determine the mass $M = \mu t_\mathrm{E}/\kappa\pi_\mathrm{E}$. Although this limit does not strictly apply, an ensemble of π_E measurements would constrain the mass function very well (Han & Gould 1995).

There are two broad classes of methods by which parallax might be measured. The first is to make a single time series from an accelerated platform, either Earth (Gould 1992; Alcock et al. 1995; Poindexter et al. 2005), or a satellite in low-Earth (Honma 1999) or geosynchronous (Gould 2013) orbit. The second is to make simultaneous observations from two (or more) observatories, either on two platforms in solar orbit (Refsdal 1966), or located at several places on Earth (Hardy & Walker 1995; Holz & Wald 1996; Gould 1997). However, with one exception, all of these methods are either subject to extremely heavy selection bias or are impractical for the present and near future. In particular, out of more than 10,000 microlensing events discovered to date, fewer than 100 have π_E measurements derived from Earth's orbital motion, and these are overwhelmingly events due to nearby lenses and with abnormally long timescales (e.g., Table 1 of Gould et al. 2010). Only two events have terrestrial parallax measurements (Gould et al. 2009; Yee et al. 2009), and Gould & Yee (2013) showed that these are subject to even more severe selection so that even the two recorded measurements is unexpectedly high.

Hence, the only near-term prospect for obtaining a statistical sample of microlens parallaxes from which to derive an unbiased mass function, as originally outlined by Han & Gould (1995), is by combining Earth-based observations with those of a satellite in solar orbit. There are several major benefits to such a study. First, it is the only way to obtain a mass-based census of stellar, remnant, and planetary populations. Several components of this population are dark or essentially dark including free-floating planets, brown dwarfs, neutron stars, and black holes and therefore are essentially undetectable by any other method unless they are orbiting other objects. In addition, even the luminous-star mass function of distant populations (e.g., in the Galactic Bulge) is substantially more difficult to study photometrically than is generally imagined. For example, a large fraction of stars are fainter components in binary systems, with separations that are too small to be separately resolved, but whose periods are too long (or primaries too faint) for study by the radial velocity technique.

In 2014, we were granted Director's Discretionary Time for a 100 hr pilot program to determine the feasibility of using *Spitzer* as such a parallax satellite for microlenses observed toward the Galactic Bulge. The main objective of this program was to measure lens masses

in planetary events. However, especially in view of the fact that there is generally no way to distinguish such planetary events from single-lens events in advance, a secondary goal was to obtain parallaxes for an ensemble of single-lens events. Prior to this program, there had been only one space-based parallax measurement, which was for a binary lens toward the Small Magellanic Cloud (Dong et al. 2007).

Here we report on the first space-based parallax measurement of an isolated lens, OGLE-2014-BLG-0939L. This measurement serves as a pathfinder and as a benchmark to test ideas that have been discussed in the literature for almost 50 years about how to resolve degeneracies in such events.

1.1. Degeneracies in Space-Based Microlens Parallaxes

As already pointed out by Refsdal (1966), space-based microlensing parallaxes are subject to a four-fold discrete degeneracy. This is because, to zeroth order, the satellite has a fixed separation from Earth projected on the plane of the sky $\mathbf{D}_\perp$, and hence they measure identical Einstein timescales $t_{\rm E} = t_{\rm E,sat} = t_{\rm E,\oplus}$. Since the flux evolution $F(t)$ of a single-lens microlensing event is given by (Paczyński 1986),

$$F(t) = F_S A(t) + F_B; \qquad A[u(t)] = \frac{u^2+2}{\sqrt{u^4+4u^2}}; \qquad [u(t)]^2 = u_0^2 + \frac{(t-t_0)^2}{t_{\rm E}^2}, \tag{4}$$

they are therefore distinguished only by different times of peak t_0 and different impact parameters u_0 (in addition to the nuisance parameters F_S and F_B, the source and blended-light fluxes, respectively). The microlens parallax $\boldsymbol{\pi}_{\rm E}$ can nominally be derived from these differences,

$$\boldsymbol{\pi}_{\rm E} = \frac{\rm AU}{D_\perp}\Big(\frac{\Delta t_0}{t_{\rm E}}, \Delta u_0\Big), \tag{5}$$

where $\Delta t_0 = t_{0,\rm sat} - t_{0,\oplus}$, $\Delta u_0 = u_{0,\rm sat} - u_{0,\oplus}$, and where the x-axis of the coordinate system is set by the Earth-satellite vector $\mathbf{D}_\perp$. The problem is that while Δt_0 is unambiguously determined from this procedure, u_0 is actually a signed quantity whose amplitude is recovered from simple point-lens events but whose sign is not (since it appears only quadratically in Equation (4)). Hence, there are two solutions $\Delta u_{0,-,\pm} = \pm(|u_{0,\rm sat}| - |u_{0,\oplus}|)$ for which the satellite and Earth observe the source trajectory on the same side of the lens as each other (with the "±" designating which side this is), and two others $\Delta u_{0,+,\pm} = \pm(|u_{0,\rm sat}| + |u_{0,\oplus}|)$ for which the source trajectories are seen on opposite sides of the lens (Gould 1994, Figure 1).

For most applications, only the second of these two degeneracies is important. That is, the two solutions $\Delta u_{0,-,\pm}$ have the same amplitude of parallax $\pi_{\rm E}$ (as do the two solutions

$\Delta u_{0,+,\pm}$) and so yield the same lens mass and distance. In each case, the solutions differ only in the direction of lens-source motion, which is usually not of major interest. However, the two sets of solutions can yield radically different $\pi_{\rm E}$. Hence, if these sets of solutions really cannot be distinguished, the value of the parallax measurement is seriously undermined. As a result, considerable work has been applied over two decades to figuring out how to break these degeneracies.

Before reviewing this work, however, one should note an important exacerbation of the underlying problem. If the four solutions are placed in the $(\Delta t_0/t_{\rm E}, \Delta u_0)$ plane, they of course all lie along a vertical line of constant Δt_0. As pointed out by Gould (1995), the error ellipses are also elongated in the vertical direction. This is because u_0 is strongly correlated with the nuisance parameters F_S and F_B (since all three enter Equation (4) symmetrically in $(t-t_0)$) while t_0, which enters anti-symmetrically, is not strongly correlated with other parameters. This continuous degeneracy enhances the probability that the discretely degenerate solutions will overlap and become a continuous degeneracy.

Four ideas have been proposed to break the Δu_0 four-fold degeneracy.

1.1.1. Measurement of $\Delta t_{\rm E}$

Gould (1995) proposed to break the degeneracy by using the fact that the Earth-satellite separation changes with time, and therefore $t_{\rm E,sat} \neq t_{\rm E,\oplus}$. For near-circular, near-ecliptic orbits (characteristic of both *Spitzer* and *Kepler*), this works quite well for targets near the ecliptic poles (Boutreux & Gould 1996) because the difference in timescales $\Delta t_{\rm E}$ is directly proportional to Δu_0. However, it becomes increasing problematic for targets close to the ecliptic, like the Galactic Bulge (Gaudi & Gould 1997), because for targets directly on the ecliptic, $\Delta t_{\rm E}$ does not depend at all on Δu_0 to linear order. That is, Δu_0 completely disappears from Equation (2.3) of Gould (1995).

1.1.2. Photometric Alignment of Space and Ground Observations

Gould (1995) also proposed to equip the satellite with a camera having identical photometric response to one on the ground, which would guarantee that $F_{S,\rm sat} = F_{S,\oplus}$ and so effectively insulate $\Delta u_{0,-,\pm}$ from uncertainties in F_S by forcing the two $\Delta u_{0,-,\pm}$ solutions to move together in a highly-correlated way as F_S is varied over its allowed range. While this idea would be quite difficult to implement, Yee et al. (2012) demonstrated that observations in different bands could be aligned quite tightly with each other based on color-color diagrams of reference stars. As a practical matter, it is not obvious that this technique can be applied to *Spitzer* observations because Yee et al. (2012) predicted F_S for a certain band by *interpolating* between two other measured bands, whereas predicting *Spitzer*'s 3.6 μm F_S

requires considerable *extrapolation* from ground-based bands.

1.1.3. Combining 1-D Parallaxes from Space and Ground

Gould (1999) suggested that the robust one-dimensional (1-D) parallax information along the $\mathbf{D}_\perp$ (i.e., Δt_0) direction from Earth-satellite observations could be combined with robust 1-D information along the direction of Earth's projected acceleration from ground-based observations (Gould et al. 1994) to break the Δu_0 degeneracy. This idea was specifically motivated by the possibility of *Spitzer* parallax observations toward the Magellanic Clouds, which are at high ecliptic latitude where these two directions are nearly orthogonal. As he noted, it is substantially more difficult to apply this approach toward the Bulge where the two directions are close to parallel.

1.1.4. High-Magnification Events (As Seen From Earth)

Gould & Yee (2012) pointed out that for sufficiently high-magnification events as observed from Earth ($|u_{0,\oplus}| \ll 1$), we have $|u_{0,\oplus}| \ll |u_{0,\rm sat}|$ and therefore $|\Delta u_{0,-,\pm}| \simeq |\Delta u_{0,+,\pm}|$, so that there is no degeneracy in the amplitude of $\boldsymbol{\pi}_{\rm E}$, although the direction degeneracy persists. Moreover, if one of the satellite observations were actually made near $t_{0,\oplus}$, then only 1–3 satellite observations would be required. They therefore advocated targeting such events. However, since OGLE-2014-BLG-0939 was not a high-magnification event, this idea is not directly relevant here and is included only for completeness.

Because this is the first space-based parallax measurement for a single-lens event, we systematically study the role of all these ideas (except the last) for both characterizing and breaking the degeneracies in practice. We note at the outset that two of these methods are adversely affected by the Bulge being close to the ecliptic, and that this problem is more pronounced for OGLE-2014-BLG-0939 than for typical events because it lies just $+2.0°$ from the ecliptic, i.e., about 3 times closer to it than Baade's Window.

2. Observations

2.1. OGLE Observations

On 2014 May 28, the Optical Gravitational Lens Experiment (OGLE) alerted the community to a new microlensing event OGLE-2014-BLG-0939 based on observations with the 1.4 deg^2 camera on its 1.3m Warsaw Telescope at the Las Campanas Observatory in Chile using its Early Warning System (EWS) real-time event detection software (Udalski et al. 1994; Udalski 2003). Most observations were in I band, but with three V band observations during the magnified portion of the event to determine the source color. At equatorial coordinates (17:47:12.25, −21:22:58.7), this event lies in OGLE field BLG630, which implies

that it is observed at relatively low cadence, roughly once per two nights.

2.2. Spitzer Observations

The structure of our *Spitzer* observing protocol is described in detail in Section 3.1 of Udalski et al. (2014). In brief, observations were made during 38 2.63 hr windows between HJD′ ≡HJD−245000 = 6814.0 and 6850.0. Each observation consisted of six dithered 30s exposures in a fixed pattern using the 3.6 μm channel on the IRAC camera. Observation sequences were upload to *Spitzer* operations on Mondays at UT 15:00, for observations to be carried out Thursday to Wednesday (with slight variations). As described in Udalski et al. (2014), JCY and AG balanced various criteria to determine which targets to observe and how often. In general, there were too many targets to be able to observe all viable targets during each epoch.

At the decision time (June 2 UT 15:00, HJD′ 6811.1) for the first week of *Spitzer* observations, OGLE-2014-BLG-0939 was poorly understood, with acceptable fits having Earth-based peaks over the range $6807 \lesssim t_{0,\oplus} \lesssim 6845$, i.e., from well before to (effectively, see below) the end of the *Spitzer* observing interval. Nevertheless, it was put in the "daily" category and observed during all eight epochs, in part because the source was bright, implying good precision *Spitzer* photometry. The following week, it was degraded to "low" priority because it was unclear that it would have low enough u_0 for an effective parallax measurement, and if u_0 were low enough, the peak would be well in the future. However, due to a transcription error, it was left in the "daily" file and observed during all six epochs. By upload time for the third week it was clear first that $t_{0,\oplus}$ would occur during or near these observations and second that the amplitude would be low (i.e., relatively high impact parameter $u_{0,\oplus} \sim 1$). These considerations pulled in opposite directions, resulting in "moderate" priority and so observations during six out of eight epochs. The fact that the predicted peak (from Earth) was expected to occur at the beginning of the fourth week led to classifying the event as "daily", and so it was observed in all seven epochs. Because OGLE-2014-BLG-0939 lies relatively far to the West, it moved out of the *Spitzer* observing window (set by the Sun-angle) during the final week. Hence it was observed during all four of the available epochs (out of eight total). Hence, OGLE-2014-BLG-0939 was observed relatively uniformly, close to once per day, during the entire interval that it was observable, from 6814.1 to 6845.7.

3. Lightcurve Analysis

The analysis of the lightcurve is straightforward because the magnification for a single-lens can be written in closed form (Equation (4)), i.e., $A = (u^2+2)/(u^4+4u^2)^{1/2}$. While the

argument u in this equation is not as simple as in the case of rectilinear motion illustrated in Equation (4), the deviations from that formula due to Earth's motion are easily incorporated (Gould 2004). *Spitzer*'s offset from the center of Earth is treated just as any other observatory, except that it is much larger, i.e., of order AU rather than $R_\oplus$. We adopt the inertial frame that is coincident with the position and velocity of Earth at the peak of the event, i.e., $\mathrm{HJD}' = 6836.06$. Any frame will yield equivalent results (after a suitable transformation of parameters). However, this (quite standard) geocentric frame permits direct comparison with the results from Earth-only observations, which turns out to be crucial to understanding the degeneracies.

As expected (Refsdal 1966), the fit yields four distinct minima, which are listed in Table 1. The best fit is shown in Figure 1. The remaining three fits look almost identical and so are not shown to avoid clutter.

We note that the degeneracy between the $\Delta u_{0,-,\pm}$ and $\Delta u_{0,+\pm}$ is marginally broken, with the latter two disfavored by $\Delta\chi^2 = 8$ and 17, respectively. However, the two $\Delta u_{0,-,\pm}$ solutions are consistent with each other at $< 1\,\sigma$.

In Table 1, we have fit with blending as a free parameter for both observatories. The results show that for the preferred solutions, the best-fit blending for OGLE is negative but consistent with zero at the $1\,\sigma$ level. A low level of negative blending is permitted because the baseline photometry is carried out against a mottled background of unresolved turnoff stars, and the source can in principle land on a "hole" in this background. However, plausible levels of negative blending due to this effect are $F_S \sim -0.2$ (on a flux scale of $I = 18$ corresponding to one flux unit), which is an order of magnitude smaller than what is observed. The most likely explanation is that the blending is very small or zero and has fluctuated below zero in the fit because of the relatively large errors in this quantity, which are typical for low-amplitude microlensing events.

In addition to the parameter values, in Table 1 we also list the heliocentric projected velocity $\tilde{\mathbf{v}}_{\rm hel}$,

$$\tilde{\mathbf{v}}_{\rm hel} = \tilde{\mathbf{v}}_{\rm geo} + \mathbf{v}_{\oplus,\perp}; \qquad \tilde{\mathbf{v}}_{\rm geo} = \frac{\boldsymbol{\pi}_{\rm E,geo}}{\pi_{\rm E}^2}\,\frac{\rm AU}{t_{\rm E,geo}}, \tag{6}$$

where $\mathbf{v}_{\oplus,\perp}(\mathrm{N},\mathrm{E}) \simeq (-0.5, 28.9)\,\mathrm{km\,s^{-1}}$ is the projected velocity of Earth at the peak of the event and where we have explicitly noted that $\boldsymbol{\pi}_{\rm E}$ and $t_{\rm E}$ are evaluated in the geocentric frame (as in Table 1). Figure 2 shows the projected velocities and $1\,\sigma$ error ellipses for each of the four solutions.

We also show in Table 2 the parameter values and errors under the assumption that $F_B = 0$. As expected from the fact that F_B was consistent with zero, the central values hardly change after application of this restriction. Note also that while the errors in u_0,

$t_{\rm E}$, and $\pi_{{\rm E},E}$ (all of which are strongly correlated with F_B) shrink dramatically under this assumption, the errors in $\tilde{\mathbf{v}}_{\rm hel}$ hardly change. This is because the East component of $\tilde{\mathbf{v}}_{\rm hel}$ (the one that is heavily correlated with $t_{\rm E}$) is directly determined from Δt_0 together with the physical separation between *Spitzer* and Earth at the times of the respective peaks, both of which are direct empirical quantities, which do not depend on the fitted Einstein timescale $t_{\rm E}$.

4. Interpretation

Here we illustrate the power of measuring $\pi_{\rm E}$ for estimating the mass and distance, even when $\theta_{\rm E}$ is not measured or constrained by considering the specific example of OGLE-2014-BLG-0939.

The $\Delta u_{0,-\pm}$ solutions are significantly favored by χ^2 so we consider these first. The solutions are nearly identical except that u_0 and $\pi_{{\rm E},N}$ reverse sign. This is expected under the "ecliptic degeneracy" (Skowron et al. 2011), which is particularly strong in the present case because the source lies only 2° from the ecliptic.

The magnitude of $\tilde{v}_{\rm hel} \sim 250\,{\rm km\,s^{-1}}$ strongly favors a Galactic disk lens at intermediate distances, an inference that follows from the relation between $\tilde{\mathbf{v}}$ and $\boldsymbol{\mu}$

$$\boldsymbol{\mu} = \frac{\tilde{\mathbf{v}}}{\rm AU}\pi_{\rm rel}. \tag{7}$$

If the lens were in the Bulge ($\pi_{\rm rel} \lesssim 0.02$), then this would imply relative proper motion $\mu_{\rm hel} = 1.05\,{\rm mas\,yr^{-1}}(\pi_{\rm rel}/0.02)$. This compares to typical Bulge lens-source proper motions $\mu \sim 4\,{\rm mas\,yr^{-1}}$. Since the probability of an event scales $\propto \mu^2$, Bulge lenses are strongly disfavored but not ruled out by this argument. On the other hand, for nearby lenses ($\pi_{\rm rel} \simeq \pi_L$), the projected velocity $\tilde{\mathbf{v}}$ is nearly equal to the space velocity of the lens in the frame of the Sun, $\mathbf{v}_\perp$. Since there are very few stars moving at these speeds, this hypothesis is also disfavored.

At intermediate distances, we would expect that the lens-source motion would be dominated by the fact that both the observer and lens partake in the same flat rotation curve. Thus, apart from the peculiar motion of the Sun and the lens (and random "noise" introduced by the proper motion of the source), we expect the lens to be moving in the direction of Galactic rotation ($\sim 30°$ East of North) at the proper motion of SgrA*, $\mu_{{\rm sgrA}*} = 6.4\,{\rm mas\,yr^{-1}}$. In fact, one of these two solutions ($\Delta u_{0,-,-}$) does show motion similar to this direction (52° East of North), making it the preferred solution.

To make a more precise comparison between the expected and observed heliocentric motions, we measure the proper motion of the "source" (actually the "baseline object" that

is coincident with the source) using four years of OGLE-IV data. We find,

$$\boldsymbol{\mu}_{S,\rm hel}(\rm N,E) = (-0.64 \pm 0.45, -5.31 \pm 0.45)\,\rm mas\,yr^{-1}. \tag{8}$$

In principle it is possible that this "baseline object" is a blend of two or more stars. However, because the blending F_B from the microlensing fit is consistent with zero and because the surface density of stars that are bright enough to substantially affect the proper motion measurement is small, we tentatively assume that the proper motion of the microlensed source and this "baseline object" are the same.

Thus, ignoring the peculiar motion of the lens, we then expect

$$\boldsymbol{\mu}_{\rm exp,hel} = \mu_{\rm sgrA*}\hat{\boldsymbol{\phi}} - \boldsymbol{\mu}_{S,\rm hel} = (6.2 \pm 0.5, 8.5 \pm 0.5)\,\rm mas\,yr^{-1} \tag{9}$$

where $\hat{\boldsymbol{\phi}}$ is the direction of Galactic rotation. The direction of this proper motion $53.9^\circ \pm 2.7^\circ$ East of North. We show immediately below that when account is taken of the dispersion in lens peculiar motions, the error bar widens to

$$\tan^{-1}\frac{\mu_{\rm exp,hel,E}}{\mu_{\rm exp,hel,N}} = 53.9^\circ \pm 8.5^\circ. \tag{10}$$

This $1\,\sigma$ range of proper motions is shown on Figure 2, which demonstrates that $\boldsymbol{\mu}_{\rm exp,hel}$ agrees extremely well with $\tilde{\mathbf{v}}_{\rm hel}$ for the $\Delta u_{0,-,-}$ solution, and disagrees with all the other solutions. Of the three other solutions, only $\Delta_{0,+,-}$ has a direction of $\tilde{\mathbf{v}}_{\rm hel}$ even remotely close to $\boldsymbol{\mu}_{\rm exp,hel}$, and this solution is disfavored by $\Delta\chi^2 = 17$ (see Tables 1 and 2, and Section 5.2, below).

Therefore, the degeneracy is decisively broken by the combination of the measurement of the source proper motion $\boldsymbol{\mu}_S$ and the fact that the value of $\tilde{v}_{\rm hel}$ strongly indicates that the lens is in the Galactic disk. This is a new form of degeneracy breaking that was not previously anticipated.

We then apply Equation (7) to derive

$$\pi_{\rm rel} \sim \mu_{\rm exp,hel}\frac{\rm AU}{\tilde{v}_{\rm hel}} = 0.20\,\rm mas, \qquad M = \frac{\pi_{\rm rel}}{\kappa\pi_{\rm E}^2} \sim 0.23\,M_\odot \qquad (\Delta u_{0,-,-}). \tag{11}$$

Note that by inserting $\mu_{\rm exp,hel}$ into the first expression in Equation (11), we are essentially applying the method described in Section 1 (paragraph below Equation (3)), except that we are making a more precise estimate of $\mu_{\rm hel}$, which is possible because the lens is already identified as being in the disk and because we have a measurement of the source proper motion.

What is the precision of these estimates? The error in the expected proper-motion estimate along the direction of motion is about 5%, while the error in $\tilde{\mathbf{v}}_{\rm hel}$ in this direction

is about 8%. The direction of motion is inclined $\sim 22^\circ$ to the Galactic plane. Adopting dispersion of $18\,\mathrm{km\,s^{-1}}$ perpendicular to and $33\,\mathrm{km\,s^{-1}}$ parallel to the Galactic plane, we derive dispersions of $20\,\mathrm{km\,s^{-1}}$ perpendicular to and $30\,\mathrm{km\,s^{-1}}$ parallel to the direction of motion. These must be multiplied by $\pi_L/\pi_{\rm rel} \sim 1.6$ to project them on the observer plane, i.e., $32\,\mathrm{km\,s^{-1}}$ and $48\,\mathrm{km\,s^{-1}}$, respectively. The former was added in quadrature to the proper motion measurement error to obtain the error bar in Equation (10). The latter contributes 19% to the error in the comparison of amplitudes. Combining these in quadrature yields $\pi_{\rm rel} = 0.20 \pm 0.04\,\mathrm{mas}$, or $D_L = 3.1 \pm 0.4\,\mathrm{kpc}$. The error in M can be estimated from $4GM/c^2 = \tilde{v}_{\rm hel}\mu_{\rm hel}t^2_{\rm E,hel}$. The first two terms have the same fractional error as above (25%), with only a very small fraction of this contributed by the lightcurve. Therefore it is appropriate to treat the error in the last term (18%) as uncorrelated, which yields $M = 0.23 \pm 0.07\,M_\odot$.

5. Degeneracies and Degeneracy-Breaking Information From the Lightcurve

As discussed in Section 4, we have decisively broken the four-fold degeneracy by measuring the source proper motion $\boldsymbol{\mu}_S$ and taking advantage of the fact that the lens lies in the Galactic Disk, which has well-organized motion. However, it is also useful to ask how well this degeneracy can be broken from lightcurve information alone since, in general, source proper motion measurements can be very difficult or impossible and not all lenses are in the Galactic Disk (or, more importantly, can be localized as being in the Disk).

5.1. Four-Fold Degeneracy

Figure 3 (modeled on Figure 1 of Gould 1994) gives a schematic view of the major sources of information that go into the parallax measurement and thus into the origins of the discrete and continuous degeneracies. The larger "ellipses" (which are so flattened that they look like line segments) represent the measurements of t_0 and u_0 based on a fit to OGLE data assuming rectilinear lens-source relative motion, i.e., according to Equation (4). Properly speaking, we should plot results of a similar fit for the *Spitzer* lightcurve. However, because there are no wing or baseline data from *Spitzer*, such a fit would be extremely poorly constrained. Instead, we therefore plot the results of a fit with the *Spitzer* timescale fixed at the best-fit OGLE value. This is legitimate because in the combined fit to the data, the *Spitzer* timescale is very tightly constrained by the OGLE timescale, although the constraint is slightly offset from equality due to Earth-*Spitzer* relative motion and lens-source relative parallax. The parameters of these single-observatory (OGLE or *Spitzer*) fits are listed in Table 3.

Within the framework of this diagram, any line segment can be drawn from an OGLE ellipse to a Spitzer ellipse. The length of this line segment relative to the radius of the Einstein

ring (large circle) corresponds to the length of Earth-*Spitzer* projected separation $\mathbf{D}_\perp$ relative to the projected Einstein radius $\tilde{r}_{\rm E} \equiv {\rm AU}/\pi_{\rm E}$. That is, $\pi_{\rm E} = (\Delta t_0^2/t_{\rm E}^2 + \Delta u_0^2)^{1/2}{\rm AU}/D_\perp$. Similarly, the direction of the line segment gives the direction of $\boldsymbol{\pi}_{\rm E}$ according to Equation (5). Four classes of line segments can be drawn, corresponding to the four-fold degeneracy. In addition, within each class, there is some freedom (primarily in the vertical direction to place the line segments within the two error ellipses. Not represented in this diagram is the fact that Einstein timescale $t_{\rm E}$ also has an error bar, so that while Δt_0 is extremely well determined, the fractional error in $\Delta t_0/t_{\rm E}$ (the quantity going into $\boldsymbol{\pi}_{\rm E}$) is basically the same as the fractional error in $t_{\rm E}$. Nevertheless, since such errors are usually modest ($\sim 10\%$ in the present case), the fractional errors in Δu_0 are likely to be larger, particularly for $\Delta u_{0,-\pm}$. Thus, Δu_0 direction is generically most problematic both because it suffers from a four-fold discrete degeneracy and because each of the four local error ellipses are elongated in the Δu_0 direction.

5.2. Degeneracy-Breaking Information

There are two striking differences between the full solution presented in Table 1 and the schematic solution presented in Figure 3 and Table 3. First, many of the geocentric parameters in Table 1 are better constrained than the OGLE-only parameters in Table 3. This includes u_0, $t_{\rm E}$, and especially F_S and F_B. These parameters are strongly correlated, so it is not surprising that if the errors in one are improved, then all will be improved. Nevertheless, this result is puzzling because the OGLE and *Spitzer* data appear to couple only through $t_{\rm E}$, and we have already noted that the *Spitzer* data by themselves contain virtually no information about $t_{\rm E}$.

Second, from the standpoint of the simple Paczyński (1986) fits that are tabulated in Table 3 and whose differences are displayed in Figure 3, the $u_{0,+,\pm}$ and $u_{0,-,\pm}$ solutions appear equally good. That is, the $\pm u_0$ solutions shown at the top and bottom of Figure 3 produce *exactly* the same lightcurve in Equation (4), so there cannot be any χ^2 difference between one combination of these and another. However, according to Table 1, the $u_{0,-,\pm}$ solutions are clearly preferred.

What is the source of additional information that reduces the parameter errors and discriminates between the four discrete solutions when the two lightcurves are fit simultaneously relative to when they are fit separately?

The answer cannot be either of the two previous suggestions that were summarized in Sections 1.1.1 and 1.1.3. As just noted, the *Spitzer* data by themselves contain essentially no timescale information, so $\Delta t_{\rm E}$ cannot be measured and hence cannot be used to discriminate among solutions with different Δu_0. In addition, because the field lies extremely close to

the ecliptic, $\Delta t_{\rm E}$ would give information about the parallax in a direction that is very nearly parallel to Δt_0 (i.e., $\mathbf{D}_\perp$ axis). And, for the same reason (as already noted by Gould 1999), the instantaneous Earth (or satellite) acceleration is almost perfectly aligned with $\mathbf{D}_\perp$, which implies that the "1-D parallax" due to this instantaneous acceleration (Gould et al. 1994) provides almost no information about Δu_0.

For the second effect (discrimination between discrete minima) the answer turns out to be a previously unrecognized source of degeneracy-breaking information. The OGLE data, by themselves, give an extremely crude 2-D parallax measurement (due to changing acceleration of Earth over the course of the event), so crude that it would not normally be considered of any use, and indeed by itself would not be of use in the present case. However, if we fix $\pi_{{\rm E},E} = 0.24$ (the preferred value for the $\Delta u_{0,-\pm}$ solutions), the OGLE data by themselves yield $\pi_{{\rm E},N}(u_0 > 0) = 0.85 \pm 0.95$ and $\pi_{{\rm E},N}(u_0 < 0) = -0.55 \pm 0.54$, which are consistent with the fitted values from the full fit (-0.25 and $+0.22$) at the 1.2 and 1.4 sigma. However, when fixed to $\pi_{{\rm E},E} = -0.06$ (the preferred value for the $\Delta u_{0,+\pm}$ solutions), the OGLE data by themselves yield $\pi_{{\rm E},N}(u_0 > 0) = 1.15 \pm 0.91$ and $\pi_{{\rm E},N}(u_0 < 0) = -0.76 \pm 0.54$, which are in conflict with the full-solution values at $2.7\,\sigma$ and $3.9\,\sigma$, respectively. These values explain both the quantitative preference for the $\Delta u_{0,-,\pm}$ solutions and also why $\Delta u_{0,+,-}$ is substantially more disfavored than $\Delta u_{0,+,+}$.

However, this "hidden information" at most partly explains the first effect. Imposing a mathematical constraint on $\pi_{{\rm E},E}$ (to reflect the physical constraint on Δt_0 coming from the combination of data from Earth and *Spitzer*) does drive down the errors in $(u_0, t_{\rm E}, F_S, F_B)$ relative to no constraint, but the errors in these quantities are still larger than those in Table 3, which assume $\boldsymbol{\pi}_{\rm E} = 0$. Moreover, the errors in the OGLE-only $\pi_{{\rm E},N}$ measurement are an order of magnitude larger than the (local solution) errors in $\pi_{{\rm E},N}$ from the joint fit. Thus, they are useful only for discriminating between widely differing $\pi_{{\rm E},N}$ solutions but not for the modest tightening of individual solutions. Hence, the source of this aspect of the improvement remains unknown.

We do note, however, that the *relative* improvement in flux errors compared to u_0 errors is well understood. The peak flux $F_{\rm peak}$ and the baseline flux $F_{\rm base} = F_S + F_B$ are both extremely robust parameters. Hence, so is their difference:

$$F_{\rm peak} - F_{\rm base} = F_S\Bigl(\frac{u_0^2+2}{\sqrt{u_0^4+4u_0^2}} - 1\Bigr). \tag{12}$$

Treating the left-hand side of this equation as a constant and differentiating yields,

$$\frac{\delta \ln u_0}{\delta \ln F_s} = \Bigl(\frac{u_0^2+2}{\sqrt{u_0^4+4u_0^2}} - 1\Bigr)\frac{u_0(u_0^2+4)^{3/2}}{8} \to 0.48 \tag{13}$$

where the evaluation is for $u_0 = 1$. Thus we expect that the fractional improvement in F_S will be about twice as great as that in u_0.

Finally, we note that, overall, it is far more important to break the discrete degeneracy than to tighten the errors on individual solutions, so the understanding of the former that has been achieved is by the same token more important than the remaining uncertainty about the latter.

5.3. Degeneracy Breaking From $(I - [3.6])_S$ Color

As discussed in Section 1.1.2, it may in principle be possible to break the four-fold degeneracy by using external information to determine the "color" (log of the ratio of source fluxes) between bands used for observations from Earth and the satellite. In our case, this would be the $(I-[3.6])_S$ color. The usual way to determine the color of a microlensed source is regression. That is if, for example, a series of V and I flux measurements are taken at nearly the same time, $F_V(t_i) = F_{S,V}A(t_i) + F_{B,V}$ and $F_I(t_i) = F_{S,I}A(t_i) + F_{B,I}$, then without even having a model to tell one the magnifications $A(t_i)$, one can write $F_V(t_i) = aF_I(t_i) + b$, yielding $(V - I)_S = -2.5\log(a) + const.$ This also implies that any model of the lightcurve must yield very similar $(V-I)_S$ colors, assuming that there are substantial contemporaneous magnified data in these two bands.

This logic breaks down for parallax observations because one does not know a priori that the magnifications are the same for contemporaneous observations. Indeed, it is only if these magnification differ that one can measure the parallax. Thus, different solutions may have different colors. Indeed, Tables 1 and 2 show that the four solutions have substantially different instrumental $(I - [3.6])_S$ colors, which range from $(I - [3.6])_S = -1.17$ to -1.43. Immediately below, we briefly describe how we use the method of Yee et al. (2012) to measure the source color to be $(I - [3.6])_S = -1.216 \pm 0.044$. However, including this measurement into the fits does not significantly alter the χ^2 differences among the four solutions. The reason appears to be that the color errors shown in Table 1 are of the same order as the color differences between solutions, so that the solutions can accommodate constraints on the color within this range without significantly changing χ^2.

The problem would appear to be that we lack *Spitzer* baseline data, which substantially degrades the determination the $(I - [3.6])_S$ color. For instance, if we put in an artificial baseline measurement with a precision of 0.005 mag (which could, e.g., be acquired in future *Spitzer* seasons), we find that the color error from the fits is reduced by a factor ~ 3 from ~ 0.20 mag to ~ 0.07 mag. However, including both this artificial baseline measurement and our actual color measurement only increases the χ^2 difference between solutions from 8 to 10, despite the fact that both our real color measurement and our artificial baseline

measurement agree perfectly with the preferred solution, while they do not agree with the alternate solutions.

We conclude that, at least in this case, a fairly accurate $(I-[3.6])_S$ source color measurement is not of substantial value in distinguishing between solutions.

For completeness, we outline our method of measuring the $(I-[3.6])_S$ source color, which is a variant of the method used by Yee et al. (2012). In our first attempt, we constructed a $(I-[3.6])$ vs. $(V-I)$ color-color diagram by matching field stars in OGLE (V/I) and *Spitzer* ([3.6]) photometry, using the same instrumental system that was used for the lightcurve photometry. We then measured the $(V-I)_S$ source color from regression (as described above), with an error of 0.026 mag. However, because of the steep slope and significant scatter in the color-color diagram, we found this approach to be unsatisfactory.

Therefore, we used H-band data of the event taken with the ANDICAM camera on the 1.3m CTIO-SMARTS telescope, combined with OGLE I-band data to measure $(I-H)_S$, and so derived $(V-H)_S$, which has a factor two longer wavelength baseline than $(V-I)$, i.e., a factor ~ 3 compared to a factor ~ 1.5. Of course, these added steps led to larger errors in the $(V-H)_S$ color (0.044 mag), but the color-color diagram had a substantially shallower slope and also less scatter. We note that for future events, a more precise $(I-[3.6])_S$ source color could be obtained by an increased number of V and H band observations.

6. Future Mass Measurement

As we have emphasized, the ensemble of single-lens parallax measurements can be used to infer the mass function of stars (and other objects) in the field without any additional data. In the present case, we have shown that the four-fold degeneracy is broken. Whether broken, partially broken, or unbroken, the ensemble of measurements can be tested against various trial mass functions using a likelihood estimator.

However, here we point out that essentially all such parallax measurements can be turned into individual mass (and distance and transverse velocity) measurements by direct imaging of the lens. We use OGLE-2014-BLG-0939 as a concrete example.

Figure 2 shows the measured projected velocities (and $1\,\sigma$ error ellipses) of the four solutions. The essence of this new method for measuring lens masses is simply to take a late-time high-resolution image (e.g., using adaptive optics (AO)) of the source and lens after they have separated. From the measured vector separation $\Delta\boldsymbol{\theta}$ and the elapsed time Δt (and for the moment making the assumptions that the source and lens were coincident at the peak of the event and that the image is taken at the same time of year as the event),

we can then derive the heliocentric proper motion,

$$\boldsymbol{\mu}_{\rm hel} = \frac{\Delta\boldsymbol{\theta}}{\Delta t}. \tag{14}$$

Comparing the direction of this vector to the four, clearly distinct directions of the solutions shown in Figure 2 one can unambiguously pick out the correct solution. Then it is a simple matter to obtain

$$\pi_{\rm rel} = \frac{\rm AU}{\tilde{v}_{\rm hel}}\mu_{\rm hel}; \qquad M = \frac{\pi_{\rm rel}}{\kappa\pi_{\rm E}^2}. \tag{15}$$

For example, the Giant Magellan Telescope (GMT) will have a FWHM in J band of 11 mas. For typical events, the proper motion will be 3–7 mas yr^{-1}, and hence the source and lens will have separated by 2 FWHM in 3–7 yr. In particular, by the time GMT is operational (perhaps 2024), it is very likely that the lens and source of OGLE-2014-BLG-0939 will be separated enough to make this measurement.

We now address various departures from our zeroth-order assumptions. First, the lens and source are not coincident at peak but are separated by $\delta\theta = u_{0,\oplus}\theta_{\rm E}$. However, since $\theta_{\rm E} \lesssim 1\,$mas while $\Delta\theta \gtrsim 20\,$mas, this will not interfere with choosing the correct solution from comparison to Figure 2. Then, once the correct solution is known, the actual path of the lens relative to the source will also be known, allowing $\boldsymbol{\mu}_{\rm hel}$ to be correctly estimated.

Second, the followup image may not be taken at the same time of year, which would lead to parallax effects. However, since $\pi_{\rm rel} < 1\,$mas in essentially all cases, while $\Delta\theta \gtrsim 20\,$mas, this will again not interfere with choosing the correct solution, and hence allowing for proper correction of parallax effects using the known $\pi_{\rm rel}$.

Third, in a substantial minority of cases, the microlensing event will be due to the less massive (and so less luminous) member of a binary system. When the AO image is taken, the brighter companion will be mistaken for the lens, yielding an incorrect $\boldsymbol{\mu}_{\rm hel}$. Gould (2014) discusses this problem in detail for the more difficult case that a 1-D geocentric parallax has been measured (rather than the simpler 4-fold discrete degeneracy under consideration here). In the current context, this will give rise to two types of discrepancy. First, the inferred $\boldsymbol{\mu}_{\rm hel}$ will not agree with any of the directions of the four $\tilde{\mathbf{v}}_{\rm hel}$ solutions. Second, the inferred mass will not agree with the photometric estimates based on the measured brightness and inferred distance of the system. In these cases, one can take a second epoch of AO observations to measure $\boldsymbol{\mu}_{\rm hel}$ of the brighter companion. If the orbit is relatively tight (few AU, corresponding to $\lesssim 1\,$mas) then the apparent motion of the companion relative to the source will be similar to that of the lens, so the original inferred proper motion will be correct, and it will be realized that the lens was the fainter (unseen) companion. If the orbit is more than a few AU, then the proper motion of the companion between the first

and second epochs will be very similar to the proper motion of the lens during the event, so this companion proper motion can just be used for $\boldsymbol{\mu}_{\rm hel}$. In this case, one will be able to derive the projected separation of the binary as well by tracing the companion position back to the time of the microlensing event when the lens had a known position relative to the source. Note that the lack of binary signatures in the lightcurve will exclude some range of binary companions. In the case of high-magnification events, this can include several decades of projected separation (e.g., Batista et al. 2014), but even for more typical events the exclusion range can be significant.

Fourth, in general, one needs to consider the impact of binary sources. Well separated binary sources are not likely to be confused with the lens because they are unlikely to lie in one of the four directions allowed by the four-fold degeneracy. In case of doubt, these can be vetted by second-epoch observations in which they would show common proper motion with the source. Unresolved binary sources might lead to displacement of the light centroid from the position of the source. This is relatively unlikely simply because microlensing events are heavily biased toward brighter sources, while flux ratios for solar-mass binaries tend to be high. However, it is also possible to vet against this possibility by comparing the source flux derived from the lightcurve (i.e., F_S) with the observed flux in the high-resolution image, to determine whether there is any unresolved light. In sum, the possibility of contamination of the astrometric measurements by binary sources must be investigated on a case by case basis, but generally is not expected to be a major problem.

Finally, dark lenses (free-floating planets, brown dwarfs, neutron stars, black holes, and some white dwarfs) will obviously not appear in followup AO images. To understand this case, let us consider how such a non-detection would be interpreted from AO observations taken 10 years after the peak of OGLE-2014-BLG-0939. For definiteness, we will assume that if the lens were at least 20 mas from the source it would have been detected. Recall that there are basically two solutions, $\tilde{v}_{\rm hel,-\pm} = 250\,{\rm km\,s^{-1}}$ and $\tilde{v}_{\rm hel,+\pm} = 60\,{\rm km\,s^{-1}}$, with corresponding $\pi_{\rm E} \sim 0.35$ and 1.35, respectively.

Non-detection implies either that the lens is dark or that it is moving $\mu_{\rm hel} < 2\,{\rm mas\,yr^{-1}}$. In the latter case, according to Equation (15) the lens would have $(\pi_{\rm rel}, M) = (< 0.04\,{\rm mas}, < 0.04\,M_\odot)$ or $(\pi_{\rm rel}, M) = (< 0.16\,{\rm mas}, < 0.01\,M_\odot)$. Thus, if it were moving too slowly to be seen (under the glare of the source) then it would also be dark (specifically because it was substellar). Of course, this would not by itself allow one to estimate its mass: it could be dark because it is a brown dwarf or because it is a massive black hole. However, applying a likelihood function to an ensemble of such objects with microlens parallax measurements that are definitely *known* not to be luminous will enable substantially more precise reconstruction of the mass function than if the entire ensemble of detections must be considered.

To illustrate this for OGLE-2014-BLG-0939, the assumption of an $M = 5\,M_\odot$ black hole would imply $\pi_{\rm rel} = \kappa M \pi_{\rm E}^2$, which yields 5 mas and 75 mas, for $\Delta u_{0,-,\pm}$ and $\Delta u_{0,+,\pm}$, respectively. While it would be very exciting to have such a black hole passing within 200 pc (or 13 pc) of the Sun, the prior probability of this is extremely low, and it would be highly discounted by any reasonable likelihood function.

7. Conclusions

The lightcurves of OGLE-2014-BLG-0939 as seen from Earth and *Spitzer* differ dramatically, with substantially different maximum magnifications and times of maximum. As predicted by Refsdal (1966), this allows to measure the microlens parallax vector $\boldsymbol{\pi}_{\rm E}$ and corresponding projected velocity $\tilde{\mathbf{v}}$ up to a four-fold degeneracy.

In Section 4 we have developed a new way to break this degeneracy. First, we show that the *magnitude* of the projected velocity $\tilde{v}_{\rm hel} \sim 250\,{\rm km\,s^{-1}}$, by itself, strongly favors a disk lens. If the lens is then assumed to be in the disk, our measurement of the source proper motion leads to a prediction for both the magnitude and direction of the lens-source relative proper motion $\boldsymbol{\mu}_{\rm hel}$. The *direction* of $\boldsymbol{\mu}_{\rm hel}$ is then found to agree closely with that of the $\tilde{\mathbf{v}}_{\rm hel}$ of one of four solutions and is clearly inconsistent with all of the other three. The *magnitude* of $\boldsymbol{\mu}_{\rm hel}$ then yields an estimate $\pi_{\rm rel} = {\rm AU}\mu_{\rm hel}/\tilde{v}_{\rm hel} = 0.20 \pm 0.04\,{\rm mas}$ and $M = \pi_{\rm rel}/\kappa\pi_{\rm E}^2 = 0.23 \pm 0.07\,M_\odot$. This new method is very powerful, but can only be applied to the minority of events that are amenable to source proper-motion measurements.

In Section 5, we have investigated three of the four ideas for breaking this degeneracy based on photometric data alone that have been developed over the past 20 years, as discussed in Sections 1.1.1–1.1.3. The fourth idea (Section 1.1.4) is not applicable to the present case. We find that the degeneracy in the magnitude of these vectors is basically broken, but the less important degeneracy in direction remains intact. We find that the mechanism for this degeneracy breaking was not previously anticipated.

We note that the $\Delta u_{0.-.-}$ solution picked out by the proper motion argument (Section 4) is favored over the two $\Delta u_{0.+.\pm}$ solutions by $\Delta\chi^2 = 8$ and 17. While such χ^2 differences would not be completely convincing on their own, as confirmation of the already strong proper-motion argument, they are compelling. In particular, of the three solutions whose directions of $\tilde{\mathbf{v}}$ conflict with the proper motion argument, only the $\Delta u_{0,+,-}$ solution is remotely near consistency, and this is disfavored in the lightcurve fit by $\Delta\chi^2 = 17$. See Table 1 and Figure 2.

An ensemble of such microlens parallax measurements, which are currently being made under our ongoing *Spitzer* program, can measure the single-lens mass function, including dark objects. We show that this measurement could be improved substantially by high-

resolution imaging of the luminous lenses using, for example, the Giant Magellan Telescope, roughly 10 years after the *Spitzer*-Earth parallax measurement.

Work by JCY, AG, and SC was supported by JPL grant 1500811. Work by JCY was performed under contract with the California Institute of Technology (Caltech)/Jet Propulsion Laboratory (JPL) funded by NASA through the Sagan Fellowship Program executed by the NASA Exoplanet Science Institute. The OGLE project has received funding from the European Research Council under the European Community's Seventh Framework Programme (FP7/2007-2013) / ERC grant agreement no. 246678 to AU. AG and BSG. were supported by NSF grant AST 1103471 AG, BSG, and RWP were supported by NASA grant NNX12AB99G. This work is based in part on observations made with the Spitzer Space Telescope, which is operated by the Jet Propulsion Laboratory, California Institute of Technology under a contract with NASA.

REFERENCES

Alcock, C., Axelrod, T., Allsman, R.A., et al. 1995, ApJ, 454, L125

Batista, V., Beaulieu, J.-P., Gould, A., Bennett, D.P., Yee, J.C., Fukui, A., Sumi, T., & Udalski, A. 2014, ApJ, 780, 54

Boutreux, T. & Gould, A. 1996, 462, 705

Dong, S., Udalski, A., Gould, A., et al. 2007, ApJ, 664, 862

Gaudi, B.S. & Gould, A. 1997, ApJ, 477, 152

Gould, A. 1992, ApJ, 392, 442

Gould, A. 1994, ApJ, 421, L71

Gould, A. 1995, ApJ, 441, L21

Gould, A. 1997, ApJ, 480, 188

Gould, A. 1999, ApJ, 514, 869

Gould, A. 2000, ApJ, 535, 928

Gould, A. 2000, ApJ, 542, 785

Gould, A. 2004, ApJ, 606, 319

Gould, A. 2013, ApJ, 763, L35

Gould, A. 2014, JKAS, in press, arXiv:1408.0797

Gould, A. & Horne, K. 2013, ApJ, 779, 28

Gould, A., Miralda-Escudé, J. & Bahcall, J.N. 1994, ApJ, 423, L105

Gould, A. & Yee, J.C. 2012, ApJ, 755, L17

Gould, A. & Yee, J.C. 2013, ApJ, 764, 107

Gould, A., Udalski, A., Monard, B. et al. 2013, ApJ, 698, L147

Gould, A., Dong, S., Gaudi, B.S. et al. 2010, ApJ, 720, 1073

Griest, K., Alcock, C., Axelrod, T.S., et al. ApJ, 372, 79

Han, C. & Gould, A. 1995, ApJ, 447, 53

Hardy, S.J. & Walker, M.A. MNRAS, 276, L79

Holz, D.E. & Wald, R.M. 1996, ApJ, 471, 64

Honma, M. 1999, ApJ, 517, L35

Paczyński, B. 1986, ApJ, 304, 1

Paczyński, B. 1991, ApJ, 371, 63

Poindexter, S., Afonso, C., Bennett, D.P., Glicenstein, J.-F., Gould, A, Szymański, M.K., & Udalski, A. 2005, ApJ, 633, 914

Refsdal, S. 1966, MNRAS, 134, 315

Skowron, J., Udalski, A., Gould, A et al. 2011, ApJ, 738, 87

Udalski, A. 2003, Acta Astron., 53, 291

Udalski, A.,Szymanski, M., Kaluzny, J., Kubiak, M., Mateo, M., Krzeminski, W., & Paczyński, B. 1994, Acta Astron., 44, 317

Udalski, A., Yee, J.C., Gould, A., et al. 2014, ApJ, sumbitted, arXiv:1410.4219

Yee, J.C., Udalski, A., Sumi, T., et al. 2009, ApJ, 703, 2082

Yee, J.C., Svartzvald, Y., Gal-Yam, A. et al. 2012, ApJ, 755, 102

Table 1: μLENS PARAMETERS (FREE F_B)

Parameter	Unit	$u_{0,-,+}$	$u_{0,-,-}$	$u_{0,+,+}$	$u_{0,+,-}$
χ^2/dof		273.1	273.7	281.5	290.2
		/ 265	/ 265	/ 265	/ 265
$t_0 - 6800$	day	36.22	36.20	36.06	35.95
		0.11	0.11	0.11	0.11
u_0		0.922	-0.913	0.897	-0.843
		0.132	0.129	0.125	0.110
$t_{\rm E}$	day	22.87	22.99	22.91	23.87
		2.14	2.12	2.10	2.04
$\pi_{\rm E,N}$		-0.248	0.220	-1.370	1.325
		0.072	0.067	0.172	0.158
$\pi_{\rm E,E}$		0.234	0.238	-0.060	0.024
		0.028	0.030	0.025	0.018
$\tilde{v}_{\rm hel,N}$	km/s	-162.3	156.9	-55.5	54.2
		7.2	5.5	2.2	2.1
$\tilde{v}_{\rm hel,E}$	km/s	181.6	199.7	26.6	29.9
		37.2	39.5	0.7	0.8
$F_{\rm S,OGLE}$		13.20	12.95	12.51	11.09
		3.77	3.63	3.42	2.75
$F_{\rm B,OGLE}$		-2.19	-1.93	-1.49	-0.08
		3.77	3.62	3.42	2.75
$F_{\rm S,Spitzer}$		4.31	4.37	3.32	3.30
		1.10	1.12	0.72	0.69
$F_{\rm B,Spitzer}$		-0.08	-0.15	0.96	1.02
		1.21	1.22	0.81	0.79

Table 2: μLENS PARAMETERS ($F_{B,\mathrm{OGLE}} = 0$)

Parameter	Unit	$u_{0,-,+}$	$u_{0,-,-}$	$u_{0,+,+}$	$u_{0,+,-}$
χ^2/dof		273.6	274.1	281.8	290.2
		/ 266	/ 266	/ 266	/ 266
$t_0 - 6800$	day	36.22	36.20	36.07	35.95
		0.11	0.11	0.10	0.11
u_0		0.840	-0.840	0.840	-0.840
		0.002	0.002	0.002	0.002
t_E	day	24.29	24.27	23.92	23.93
		0.16	0.16	0.15	0.15
$\pi_{\mathrm{E,N}}$		-0.214	0.192	-1.292	1.321
		0.044	0.043	0.029	0.029
$\pi_{\mathrm{E,E}}$		0.217	0.222	-0.052	0.024
		0.006	0.008	0.018	0.033
$\tilde{v}_{\mathrm{hel,N}}$	km/s	-164.9	158.3	-56.4	54.3
		4.8	4.7	1.3	1.3
$\tilde{v}_{\mathrm{hel,E}}$	km/s	195.5	212.4	26.7	29.9
		34.2	36.3	0.7	0.8
$F_{\mathrm{S,OGLE}}$		11.01	11.01	11.01	11.01
		0.00	0.00	0.00	0.02
$F_{\mathrm{B,OGLE}}$		0.00	0.00	0.00	0.00
		0.00	0.00	0.00	0.00
$F_{\mathrm{S,Spitzer}}$		3.85	3.93	3.10	3.29
		0.68	0.69	0.47	0.50
$F_{\mathrm{B,Spitzer}}$		0.34	0.25	1.15	1.04
		0.87	0.88	0.64	0.66

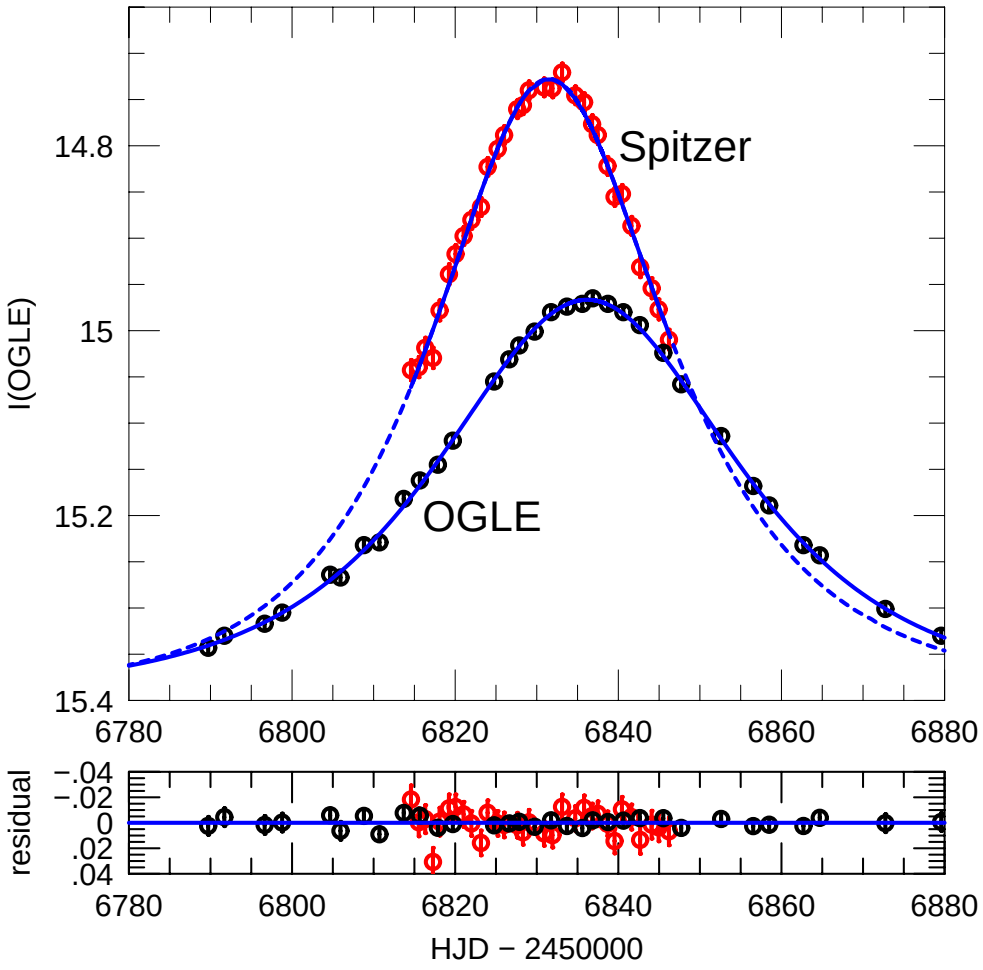

Fig. 1.— Lightcurve of OGLE-2014-BLG-0939 as seen by OGLE from Earth (black) and *Spitzer* (red) $\sim 1\,\mathrm{AU}$ to the West. While both are well-represented by Paczyński (1986) curves (blue), they have substantially different maximum magnifications and times of maximum, whose differences yield a measurement of the "microlens parallax" vector $\boldsymbol{\pi}_\mathrm{E}$. The dashed portion of the *Spitzer* curve extends the model to what *Spitzer* could have observed if it were not prevented from doing so by its Sun-angle constraints. Light curves are aligned to the OGLE I-band scale (as is customary), even though *Spitzer* observations are at $3.6\,\mu$m. Lower panel shows residuals.

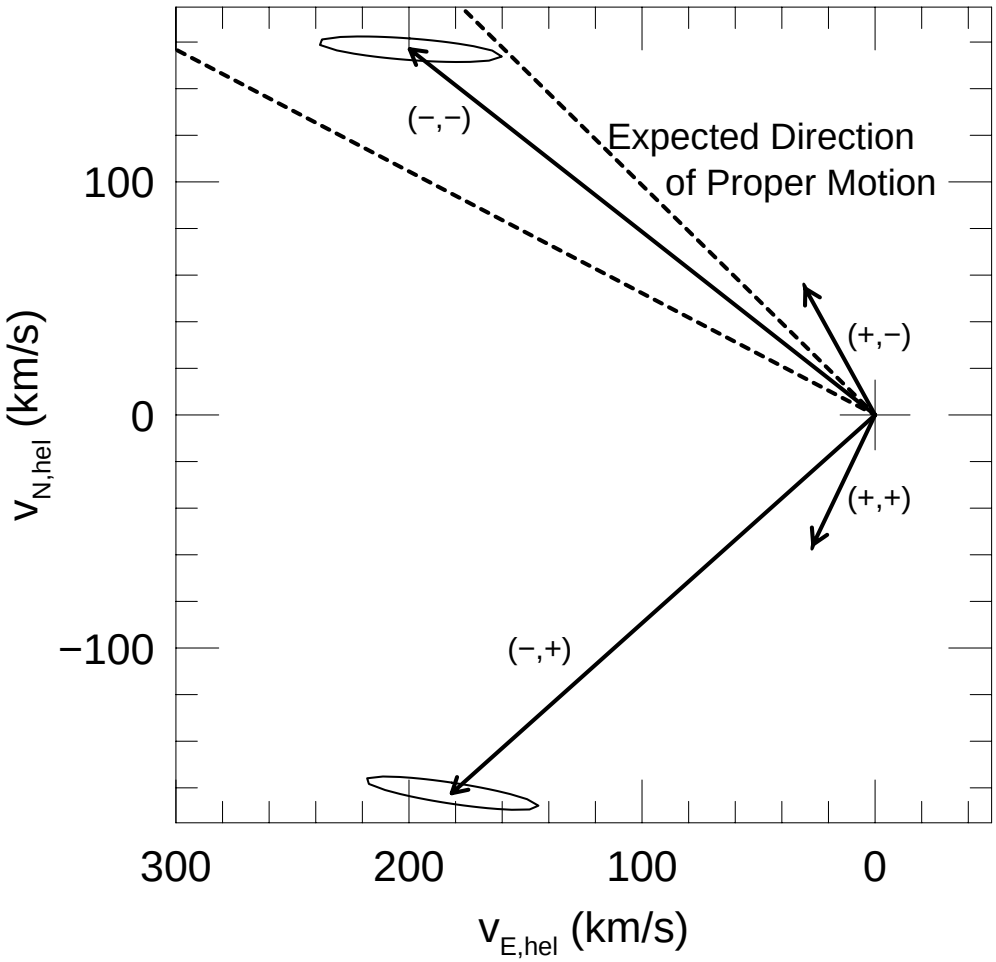

Fig. 2.— Four-fold degeneracy in the heliocentric projected velocity $\tilde{\mathbf{v}}_{\rm hel} = \tilde{\mathbf{v}}_{\rm geo} + \mathbf{v}_{\oplus,\perp}$ where $\tilde{\mathbf{v}}_{\rm geo} = \boldsymbol{\pi}_{\rm E,geo}{\rm AU}/\pi_{\rm E}^2 t_{\rm E}$ and $\mathbf{v}_{\oplus,\perp}$ is the velocity of Earth projected on the sky at the peak of the event. Solutions are labeled $(\pm,\pm)$ by their Δu_0 degeneracy. Two smaller $\tilde{v}_{\rm hel}$ $(+,\pm)$ are disfavored by $\Delta\chi^2 = 8$ and 17. Note that the error ellipses for these are quite small and partly obscured by the "arrow heads". The dashed curves show the $1\,\sigma$ error for the expected direction $\tilde{\mathbf{v}}_{\rm hel}$ (same as $\boldsymbol{\mu}_{\rm hel}$) based on the measured proper motion of the source and the assumption that the lens is in the Galactic Disk. This proper motion measurement decisively breaks the degeneracy.

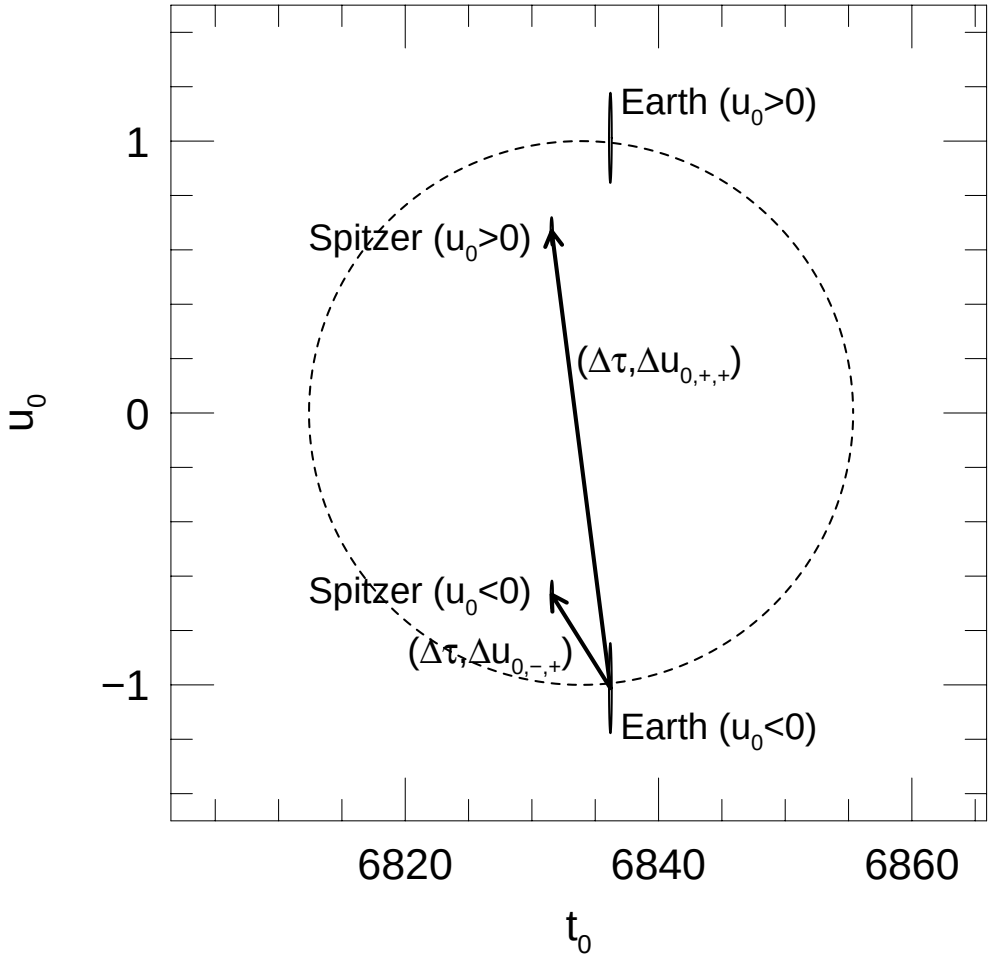

Fig. 3.— Origin of Refsdal (1966) four-fold degeneracy. Lightcurves from Figure 1 unambiguously determine peak times t_0 (abscissa) as seen from Earth and *Spitzer* but only specify u_0 (ordinate) up to a sign. Hence, there are four ways to "connect" the Earth and *Spitzer* measurements, which in each case is identified with the Earth-*Spitzer* projected separation $\mathbf{D}_\perp$ to determine the microlens parallax vector $\boldsymbol{\pi}_{\rm E}$ according to Equation (5). Dashed circle represents the Einstein radius, which brings the two axes to the same system by scaling the abscissa by the Einstein timescale $t_{\rm E}$. For each possible solution, the connecting line segment divided by $D_\perp$ is equal to $\pi_{\rm E}/{\rm AU}$. Two such line segments are shown explicitly, with $\Delta\tau \equiv \Delta t_0/t_{\rm E}$. Hence there is a four-fold degeneracy in the direction of $\boldsymbol{\pi}_{\rm E}$ but only a two-fold degeneracy in its magnitude. Error ellipses for each solution generate much smaller errors, which become important only if the discrete degeneracy is broken.

Table 3: Single-Observatory Parameters

Parameter	Unit	OGLE	Spitzer
χ^2/dof		242.9	28.0
		/ 238	/ 26
$t_0 - 6800$	day	36.20	31.57
		0.11	0.09
u_0		1.012	0.668
		0.166	0.052
$t_{\rm E}$	day	21.48	21.48
		2.31	0.00
$F_{\rm S}$		15.99	4.32
		5.47	0.81
$F_{\rm B}$		-4.98	-0.13
		5.47	1.00